Doppler Radar Analysis of the Eyewall Replacement Cycle of Hurricane Matthew (2016) in Vertical Wind Shear

TING-YU CHA,[a] MICHAEL M. BELL,[a] AND ALEXANDER J. DESROSIERS[a]

[a] *Department of Atmospheric Science, Colorado State University, Fort Collins, Colorado*

(Manuscript received 1 September 2020, in final form 14 May 2021)

ABSTRACT: Hurricane Matthew (2016) was observed by ground-based polarimetric radars in Miami (KAMX), Melbourne (KMLB), and Jacksonville, Florida (KJAX), and a NOAA P3 airborne tail Doppler radar near the coast of the southeastern United States during an eyewall replacement cycle (ERC). The radar observations indicate that Matthew's primary eyewall was replaced with a weaker outer eyewall, but unlike a classic ERC, Matthew did not reintensify after the inner eyewall disappeared. Triple-Doppler analysis was calculated from the NOAA P3 airborne fore and aft radar scanning combined with the KAMX radar data during the period of secondary eyewall intensification and inner eyewall weakening from 1900 UTC 6 October to 0000 UTC 7 October. Four flight passes of the P3 aircraft show the evolution of the reflectivity, tangential winds, and secondary circulation as the outer eyewall became well established. Further evolution of the ERC is analyzed from the ground-based single-Doppler radar observations for 35 h with high temporal resolution at a 5-min interval from 1900 UTC 6 October to 0000 UTC 8 October using the Generalized Velocity Track Display (GVTD) technique. The single-Doppler analyses indicate that the inner eyewall decayed a few hours after the P3 flight, while the outer eyewall contracted but did not reintensify and the asymmetries increased episodically. The analysis suggests that the ERC process was influenced by a complex combination of environmental vertical wind shear, an evolving axisymmetric secondary circulation, and an asymmetric vortex Rossby wave damping mechanism that promoted vortex resiliency despite increasing shear.

SIGNIFICANCE STATEMENT: In many tropical cyclones the eyewall where the heaviest rain and winds are found is replaced by a larger outer eyewall, leading to an expansion of the damaging winds and intensity change, but this process is not well understood. Hurricane Matthew (2016) underwent an eyewall replacement that was observed by coastal and airborne radars, but in contrast to other storms was impacted by strong vertical wind shear during the process. In this study we analyze 35 h of radar data to examine Matthew's evolution. The analyses show a complex interaction between the external vertical wind shear and the internal dynamics of the storm that weakened the storm and increased its asymmetry, improving our understanding of hurricane structure and intensity change.

KEYWORDS: Atmosphere; Hurricanes; Tropical cyclones; Mesoscale processes; Wind shear; Aircraft observations; Radars/Radar observations

1. Introduction

An eyewall replacement cycle (ERC) can cause significant changes to the intensity and structure of a tropical cyclone (TC), but the physical mechanisms involved in the ERC process are not fully understood partly due to a lack of detailed observations. While an ERC evolution has been commonly interpreted within an axisymmetric framework (Willoughby 1982; Black and Willoughby 1992; Sitkowski et al. 2011; Bell et al. 2012b), past studies suggest that asymmetries also play an significant role, and have in part documented the asymmetric internal and external forcing impacting an ERC evolution (Qiu et al. 2010; Didlake and Houze 2011; Didlake et al. 2017; Guimond et al. 2018, 2020). Still, detailed and continuous observations of the eyewall replacement processes are required in order to advance our understanding of the phenomenon. Hurricane Matthew (2016), the first category 5 hurricane in the Atlantic basin since 2007, paralleled the east coast of Florida and completed an ERC along its path. The ERC was associated with a broadening of the wind field which expanded strong winds and caused widespread damage on the Florida coastline. Given the close proximity to the coast, Matthew was observed by three Next Generation Weather Radar (NEXRAD) radars in Miami (KAMX), Melbourne (KMLB), and Jacksonville, Florida (KJAX), for 35 h with high temporal resolution, and by a NOAA WP-3D (hereafter P3) airborne tail Doppler radar (TDR) with high spatial resolution during the development of the outer eyewall. The radar observations indicate that Matthew underwent an ERC process where the primary eyewall was replaced with a weaker outer eyewall, but unlike a classic ERC (Willoughby 1982; Black and Willoughby 1992; Sitkowski et al. 2011), Matthew did not reintensify. The observations also show the presence of significant asymmetries due to increased vertical wind shear and possible land interactions throughout the process. In this study, ground-based and airborne Doppler radar simultaneous observations and continuous coastal radar surveillance provide a unique opportunity to examine the axisymmetric and low-wavenumber evolution of Matthew's ERC impacting by asymmetric forcings.

An ERC is known as one of the key processes that modulates TC intensity and structure, which most frequently happens in intense, symmetric systems (Willoughby 1982; Black and Willoughby 1992; Houze et al. 2007; Sitkowski et al. 2011;

Corresponding author: Ting-Yu Cha, tingyu@colostate.edu

DOI: 10.1175/MWR-D-20-0289.1

Bell et al. 2012b), but occasionally occurs in weaker, more asymmetric systems (Razin and Bell 2021). A key element of the structural changes of the storm during a canonical ERC is the replacement of an older, weakening inner eyewall by a newer, intensifying outer eyewall. The paradigm of a classic ERC in an axisymmetric framework in terms of the intensity change is associated with three phases: intensification (Shapiro and Willoughby 1982; Smith et al. 2009; Bell et al. 2012b), weakening (Hoose and Colón 1970; Houze et al. 2007; Rozoff et al. 2008; Bell et al. 2012b; Didlake et al. 2017) and reintensification (Sitkowski et al. 2011, 2012). While the three phases described here represent a canonical ERC, there are many variations in the process that occur in individual storms due to both environmental factors and internal axisymmetric and asymmetric dynamics.

Accurate hurricane intensity prediction requires the understanding of both axisymmetric and asymmetric dynamics (Reasor et al. 2009). Axisymmetric and asymmetric mechanisms are necessarily coupled together, such as the axisymmetrization of potential vorticity (PV) perturbations that can lead to intensification of the hurricane (Montgomery and Kallenbach 1997). Previous studies have investigated individual stages of ERCs mostly in an axisymmetric framework. Although axisymmetric mechanisms can represent important aspects of the TC dynamics, asymmetric dynamics also play a role. Didlake et al. (2017) found that Hurricane Gonzalo (2014) exhibited an azimuthal shift of convective and kinematic asymmetries in ERC evolution, which might result from the interaction with the environmental wind shear. Guimond et al. (2020) suggested that vortex Rossby waves (VRWs) contributed to Hurricane Matthew's (2016) secondary eyewall formation by spinning up the outer core tangential wind. The current study builds upon this previous work by focusing on the impact from the interaction between vertical wind shear (VWS) and VRWs during the ERC evolution in Matthew.

Environmental VWS is regarded as one of the most important environmental predictors of TC intensity changes. The vortex interaction with the environmental flow can influence TC intensity and structure through several pathways: midlevel ventilation (Tang and Emanuel 2012), convective and kinematic asymmetries (Black et al. 2002), and vortex tilt (Jones 1995). A comprehensive study with a 6-hourly dataset from 1982 to 2014 by Rios-Berrios and Torn (2017) showed that high VWS environments (above 11 m s^{-1}) often act as a hindrance to TC intensification, but that moderate VWS (4.5–11 m s^{-1}) associated with other favorable environmental factors (such as high sea surface temperature, sufficient midlevel moisture) can be conducive for TC intensification.

Convective asymmetries are highly dependent on the shear magnitude. Observations of Hurricane Jimena (1991) and Hurricane Olivia (1994) have shown that convection can organize itself into axisymmetric rings and continue to intensify in a weakly sheared environment (Black et al. 2002). However, when a TC encounters high shear, both radar reflectivity and vertical motion possess strong wavenumber-1 components, where the convection and updrafts initiate in the downshear-right quadrant of the storm and advect and mature cyclonically downstream (Corbosiero and Molinari 2003). VWS results in the strongest convection on the downshear left, with a transition to stratiform precipitation occurring when the cells reach the upshear side of the eyewall (Black et al. 2002; Hence and Houze 2012; DeHart et al. 2014; Foerster et al. 2014; Boehm and Bell 2021). As the cells propagate toward the right of shear, most hydrometeors have already either frozen or precipitated out. The unloaded cells become weaker and separate from the eyewall. Reasor et al. (2013) composited 75 TC flights and confirmed the azimuthal distribution of the convective and kinematic asymmetry impacted by the VWS on average.

VWS acts to tilt the vortex and reduce its alignment in the vertical. Vortex realignment is therefore a vital process for a TC to maintain its structure in a sheared environment, and two key mechanisms have been proposed to explain the realignment process: vortex precession (Jones 1995) and damping by VRWs (Reasor et al. 2004). Jones (1995) showed that the coupling between upper- and lower-level cyclonic PV anomalies results in cyclonic precession of the vortex, with increasing Rossby penetration depth leading to less tilting of the vortex. Increased penetration depth and reduced susceptibility of the vortex to VWS is a function of increased Coriolis parameter, reduced static stability, and increased strength or size of the vortex. Wang and Holland (1996) found that the simulated TC achieved a quasi-steady tilt in the downshear left through the realignment process.

Another mechanism for vortex realignment has been described by Reasor and Montgomery (2001), demonstrating the fundamental role of VRWs in the relaxation of a tilted vortex to an aligned state in the presence of shear. The axisymmetrization of vortex perturbations enabled by VRWs was first proposed by Montgomery and Kallenbach (1997). The emergence of VRWs has been discussed via the barotropic breakdown of an unstable ring vortex (Schubert et al. 1999) and forced by the environmental shear (Reasor et al. 2004). VRWs in the inner core propagate radially outward and stagnate at the radii where the radial vorticity gradient disappears or reverses sign (Wang 2002). The propagation of waves can change the eyewall shape and transport momentum, and they can be seen on radar imagery where the shape of the eyewall is polygonal or elliptical (Kuo et al. 1999; Cha et al. 2020). Reasor et al. (2004) has demonstrated that VRWs can act as a damping mechanism that can maintain vortex vertical alignment in a sheared environment using a simple linearized primitive equation model that was supported by Hurricane Olivia (1994) analysis. Reasor et al. (2009) and Reasor and Eastin (2012) further supported the reduction of vortex tilt by the VRW damping mechanism in response to the shear forcing using observations of Hurricane Guillermo (1997).

The above studies have suggested that a vortex can be resilient in the presence of environmental VWS due to internal vortex dynamics, but none of the previous studies has applied these concepts to the ERC process. In this study, we investigate the interaction between environmental VWS and internal vortex dynamics in Matthew's ERC, and document the axisymmetric and low-wavenumber evolution with the triple-Doppler and single-Doppler analyses. Triple-Doppler analysis from combined airborne fore and aft scanning and ground-based radars provide snapshots of the full axisymmetric wind field using a

TABLE 1. Radar observation periods and aircraft missions used in this study.

Radar analysis	Duration
Pass 1	P3: 1855–1940 UTC 6 Oct
	KAMX: 1920 UTC 6 Oct
Pass 2	P3: 2020–2105 UTC 6 Oct
	KAMX: 2039 UTC 6 Oct
Pass 3	P3: 2145–2230 UTC 6 Oct
	KAMX: 2211 UTC 6 Oct
Pass 4	P3: 2305–2340 UTC 6 Oct
	KAMX: 2323 UTC 6 Oct
KAMX radar	1907 UTC 6 Oct–0550 UTC 7 Oct
KMLB radar	0125–1800 UTC 7 Oct
KJAX radar	1307 UTC 7 Oct–0009 UTC 8 Oct

variational wind synthesis technique (Foerster et al. 2014; Foerster and Bell 2017). Continuous observations from three ground-based radars are used to retrieve Matthew's axisymmetric and asymmetric kinematic structure over the 35-h ERC process using the Generalized Velocity Track Display (GVTD) technique (Jou et al. 2008; Cha and Bell 2021). The dataset and analysis methodology are presented in section 2. A general storm life cycle and evolution are in section 3 described by the satellite, SFMR, and shear products. The results of the triple-Doppler and single-Doppler analyses in axisymmetric framework to examine the convective and kinematic structures are illustrated in section 4, and the asymmetric evolution derived from the single-Doppler analysis are presented in section 5. A summary of the results and conclusions are presented in section 6.

2. Dataset and analysis methodology

Hurricane Matthew tracked parallel to the east coast of Florida and was within range of KAMX, KMLB, and KJAX ground-based radars during its ERC. The analysis period of each radar is listed in Table 1, and the location of each radar is displayed in Fig. 1. Full radar volumes were available from each radar at approximately 5-min intervals and were processed with lidar Radar Open Software Environment (LROSE) software (Bell 2019) and were quality controlled to remove nonmeteorological echoes and correct velocity aliasing (Bell et al. 2013). The edited data were analyzed by the Vortex Objective Radar Tracking and Circulation (VORTRAC) software using the GVTD technique with an improved algorithm to retrieve the kinematic structure (Jou et al. 2008; Cha and Bell 2021). The GVTD technique is able to retrieve the axisymmetric and full asymmetric component of tangential wind from a single-Doppler radar, providing a quantitative approach to estimate the kinematic structure of TCs with high temporal resolution. Since the GVTD-retrieved wind field can be sensitive to the center location, aircraft-derived dynamic centers (Willoughby and Chelmow 1982) from the Hurricane Research Division (HRD) were utilized as stable, reference centers to perform the GVTD technique. More detailed descriptions on the GVTD technique, the uncertainty of the wind field retrieval, and

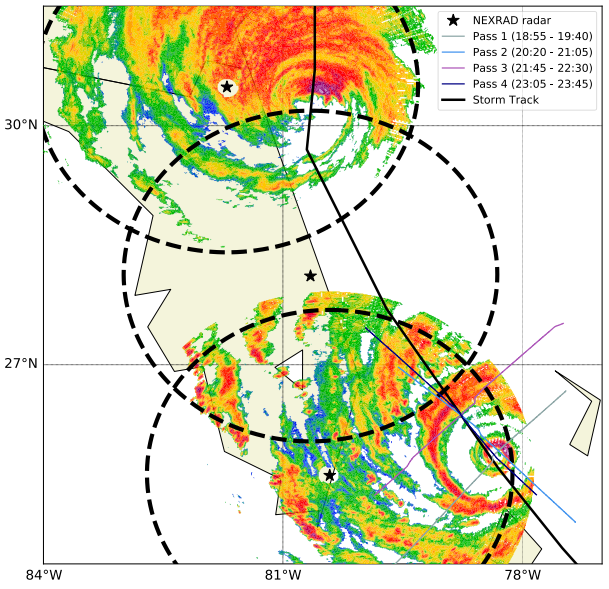

FIG. 1. Summary of Hurricane Matthew observations used in this study. Passes 1–4 denote the passage of the P3 aircraft across the cyclone center on 6 Oct. Black dashed circles and stars represent the detecting range (230 km) and location of each single-Doppler radar (KAMX, KMLB, and KJAX from south to north, respectively). The black solid line represents the storm track. Shading denotes the reflectivity at 4-km altitude at 1930 UTC 7 Oct and 2126 7 Oct from south to north, respectively.

the maximum allowable data gap to retrieve each wavenumber can be found in Cha and Bell (2021), Lee et al. (2000), and Lorsolo and Aksoy (2012).

Once the axisymmetric tangential and radial winds are derived at each radius and height, the axisymmetric vertical absolute vorticity is calculated as $\overline{\eta} = \overline{V_T}/r + \partial\overline{V_T}/\partial r + f$, where $\overline{V_T}$ denotes the azimuthal mean tangential wind, r denotes the radius, and f denotes the Coriolis parameter on an f-plane. The axisymmetric tangential wind is much stronger than the asymmetric tangential wind components, while the axisymmetric radial wind is more sensitive to the errors of TC center estimation and mean wind component (Lee et al. 2000). Hence, we only discuss tangential component of the wind field in this study. The NOAA P3 aircraft flew a reconnaissance mission from 1900 UTC 6 October to 0000 UTC 7 October. The P3 was equipped with a TDR operating in fore–aft scanning mode in order to obtain pseudo-dual-Doppler measurements, documenting the period of Matthew's ERC during the intensification and weakening stages. The flight track of the P3 collected data in the four passes across the TC center, with each pass 30–60 min apart. The time window for the four passes is listed in Table 1, and the location of each pass is shown in Fig. 2. The P3 radar data were first corrected for navigation errors (Cai et al. 2018) and the "medium" quality control script developed by Bell et al. (2013) was applied to the radar data to eliminate most of ground clutters and noise. Any remaining nonmeteorological noise and clutter were manually removed. A low bias in reflectivity was found comparing the X-band P3 data to the S-band KAMX radar. To ensure an accurate

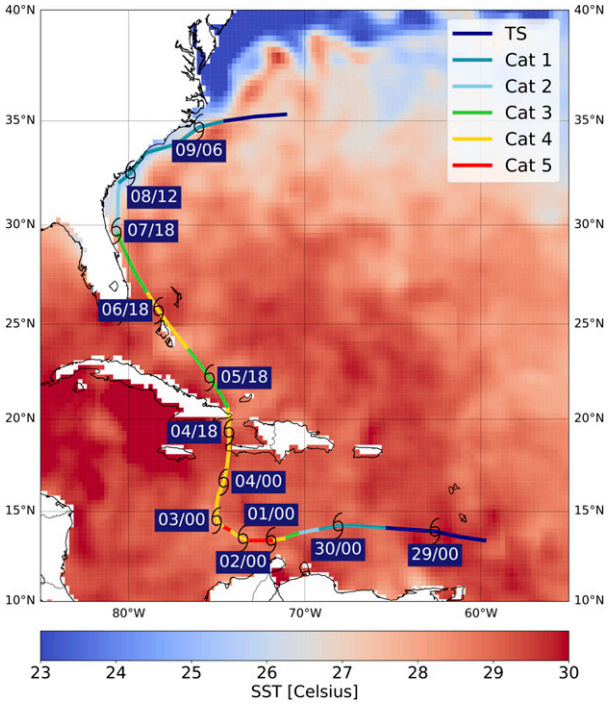

FIG. 2. Best track and intensity of Hurricane Matthew from the NHC denoted with dates and UTC times. The shading indicates the daily sea surface temperature (SST) on 7 Oct obtained from the Daily Optimum Interpolation Sea Surface Temperature dataset from the NOAA/National Centers for Environmental Information.

convective structure in the triple-Doppler analysis, the ground-based radar data were treated as a ''true'' measurement with the assumption that it was well-calibrated and did not suffer from significant attenuation. Since the KAMX radar has the limitation on the detecting range, the correction only utilized the reflectivity in the inner core of the vortex (approximately 80 km × 80 km) from the altitude of 4.5–8 km where both radars could detect. Based on the coincident KAMX and P3 observations, a constant offset of 8.375 dBZ was calculated and added to the P3 reflectivity everywhere to correct for the low bias. The specific value of the bias correction does not affect the interpretation of results since we are not analyzing quantitative precipitation estimates, but rather produces a more consistent radar depiction of the storm structure from the multiple radars.

The KAMX radar and the P3 TDR simultaneously collected the data from Hurricane Matthew from 1900 UTC 6 October to 0000 UTC 7 October. The KAMX radar has larger data coverage, but the P3 TDR has higher spatial resolution due to its closer range. The triple-Doppler analysis combined from the KAMX and P3 radar observations can provide better spatial coverage and geometry. Each pass and one volume of KAMX data were synthesized at 1-km horizontal nodal spacing and 0.5-km vertical nodal spacing with Spline Analysis at Mesoscale Utilizing Radar and Aircraft Instrumentation (SAMURAI) software (Bell et al. 2012a; Foerster et al. 2014; Foerster and Bell 2017) in LROSE. SAMURAI is a 3D variational data assimilation tool that uses a cubic b-spline basis to find the most likely state of the atmosphere given a set of observations by minimizing the difference between the observed radial velocities and the analyzed wind solution. The data spacing of the P3 TDR is approximately ~1.4 km in the along-track direction due to the rotation rate of the radar. We use a spline nodal spacing that is smaller than the data spacing to accurately resolve spatial scales appropriate for the given sampling (e.g., Koch et al. 1983; Ooyama 1987, 2002). A $4\Delta x$ low-pass Gaussian filter in the horizontal and $2\Delta x$ filter in the vertical were applied to the triple-Doppler analysis to resolve minimum scales of ~4 and ~1 km, respectively. With the selected nodal spacing and filtering, the minimum resolved scale of the wind field is approximately 2.85 times the along-track data spacing of the P3.

The analysis track for the triple-Doppler analysis was linearly interpolated from each aircraft-derived dynamic center with the given storm motion. The analysis was initially performed on a Cartesian grid and then interpolated into cylindrical coordinates with azimuthal resolution of 1°, radial resolution of 1 km, and vertical resolution of 0.5 km. To prevent isolated and insufficient data points from biasing values, a minimum of 50% azimuthal coverage was required when calculating azimuthal mean quantities.

Additional datasets used in this study include Matthew's and best track and intensity from the National Hurricane Center (NHC), and the environmental vertical shear from the Statistical Hurricane Intensity Prediction Scheme dataset (SHIPS; DeMaria et al. (2005)). The environmental VWS variable diagnosed in this study is 850–200-hPa shear with vortex removed and averaged from 0 to 500 km relative to the 850-hPa vortex center. The measurements of surface wind during the four passes are obtained from the Stepped Frequency Microwave Radiometer (SFMR; Uhlhorn et al. (2007)). The SFMR was carried by the P3 aircraft for measuring surface brightness temperature at six C-band frequencies. The estimation of surface wind speed along the flight track is derived from a geophysical model function (GMF) relating surface emissivity and wind speed.

3. Hurricane Matthew (2016)

Figure 2 shows Hurricane Matthew's track and intensity. Hurricane Matthew originated from an African easterly wave and became a tropical storm on 28 September (Stewart 2017; Laurencin et al. 2020; Guimond et al. 2020). Matthew underwent a 24-h period of rapid intensification (RI) between 0000 UTC 30 September and 0000 UTC 1 October when it passed over warm Caribbean waters and reached category 5 intensity on 1 October at 13.4° latitude, with minimum pressure of 942 hPa and maximum sustained surface winds of 145 kt. RI is defined as a increase in the maximum sustained wind of 15.4 m s^{-1} (30 kt) within 24-h (Kaplan and DeMaria 2003). Matthew set a new record as the southernmost hurricane to reach category 5 intensity at the lowest latitude in the Atlantic basin. Matthew then began to weaken while moving northward under a moderate shear environment. As Matthew made

landfall in Haiti and interacted with the mountainous region, its low-level circulation was disrupted and the intensity decreased to category 3. Matthew reintensified after the next 18 h, and reached category 4 intensity by 1200 UTC 6 October. The storm then traveled along the East Coast of the United States from 6 to 9 October, completed an ERC, and then made a right turn to the eastern Atlantic, where it dissipated. Figure 2 shows that Matthew moved over a relatively colder ocean surface on 7 October, indicating that the environment was less favorable for reintensification. Figure 3 denotes our analysis period during the weakening stage of Matthew. The overlap between the triple-Doppler and single-Doppler radar analyses is from 1900 UTC 6 October to 0000 UTC 7 October.

The 89- and 91-GHz microwave satellite imagery illustrates the convective evolution during Matthew's ERC (Fig. 4). At 2319 UTC 5 October (Fig. 4a), deep convection started to form outside the primary eyewall and a spiral banded structure became evident by 1150 UTC 6 October (Fig. 4b). The signature of a concentric eyewall where the inner eyewall was bounded by a nearly circular band of precipitation was observed at 1656 UTC 6 October (Fig. 4c). Figure 4d shows that the convection in the inner eyewall had weakened and by 1221 UTC 7 October, the inner eyewall almost disappeared and was replaced by the secondary eyewall (Fig. 4e). After the dissipation of the inner eyewall, Matthew became asymmetric and the convection was concentrated on the north side of the storm (Fig. 4f).

The VWS evolution throughout Matthew's life cycle is depicted in Fig. 3b. The deep-layer shear (850–200 hPa) magnitude was low to moderate with westerly shear through the earlier period. The shear direction changed to southwesterly around the time when Matthew initiated the ERC on 6 October. VWS strengthened rapidly near the end of the analysis period and reached 14 m s^{-1}. The local wind shear in the inner core out to 60-km radius calculated from the triple-Doppler analysis averaged u and v wind field to derive the mean wind component of each level was northwesterly at 12 m s^{-1}. The local shear was stronger and from a different direction than the environmental wind shear calculated from the SHIPS dataset, although was similar to the previous time period. We cannot separate the shear contributions from the large-scale environment and storm-scale asymmetries using the current dataset, but speculate that the discrepancy may be due to the fact that the shear was being induced by an impinging trough captured by the larger scale analysis that had not affected the inner-core yet (Stewart 2017). The difference may also be the result of modification of the local environment by the TC itself.

Figure 5 denotes the surface wind of the SFMR analysis using a 1–2–1 filter to smooth the data from passes 1 through 4. The P3 track (Fig. 1) shows that a secondary wind maximum approximately 30 m s^{-1} around the 60-km radial distance on the southwest side of the storm was detected by the SFMR during the pass 1. Wind maxima associated with the inner eyewalls along the radial flight leg were ~50 m s^{-1} in pass 2, and both sides detected a secondary wind maximum. The maximum wind in the inner eyewall then weakened from 52 to 45 m s^{-1} within 5 h on the northern side of the storm, whereas an intensifying trend of the secondary wind maximum from 30 to 36 m s^{-1} was detected. The surface wind evolution shows a broadening of the wind field and an appearance of the secondary wind maximum in the boundary layer, consistent with an ongoing ERC process (Sitkowski et al. 2011).

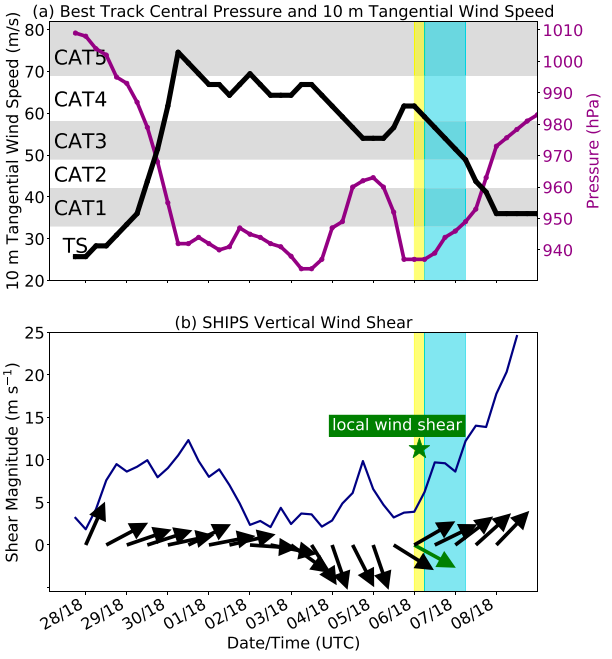

FIG. 3. (a) NHC best track central pressure (purple line) and maximum wind speed (black line) throughout the lifetime of Matthew. (b) Environmental VWS evolution. The black arrow indicates the direction of the 850–200-hPa VWS, and the blue line indicates the shear magnitude of the 850–200-hPa environmental shear. Westerly shear is associated with a 90° heading. The green arrow and star represent the local shear direction and magnitude calculated from triple-Doppler analysis averaged from 0- to 60-km radius from the aircraft-derived dynamic center. Yellow shading denotes P3 flight period and blue shading denotes single-Doppler analysis period.

4. Axisymmetric structure

a. *Triple-Doppler analysis*

Figure 6 shows the azimuthally averaged convective and kinematic structure and evolution over the four passes of the triple-Doppler analysis. The period corresponds to the end of the intensification stage and the start of the weakening stage of an ERC in which the inner eyewall weakened while the outer eyewall developed and strengthened.

At ~1900 UTC (Fig. 6a), the inner eyewall had a vertical velocity of 2.9 m s^{-1} at 11–13 km altitude, with a well-developed outflow associated with the dominant secondary circulation. The primary circulation (tangential wind) of the inner eyewall had a peak value of 53 m s^{-1}, extending vertically to 4-km altitude. The "moat" was delineated by no reflectivity region (between 35- and 45-km radius). In the outer eyewall region (between 50- and 75-km radius), the convection was broad and shallow, with a maximum of 0.7 m s^{-1} vertical velocity and 38.3 m s^{-1} tangential velocity.

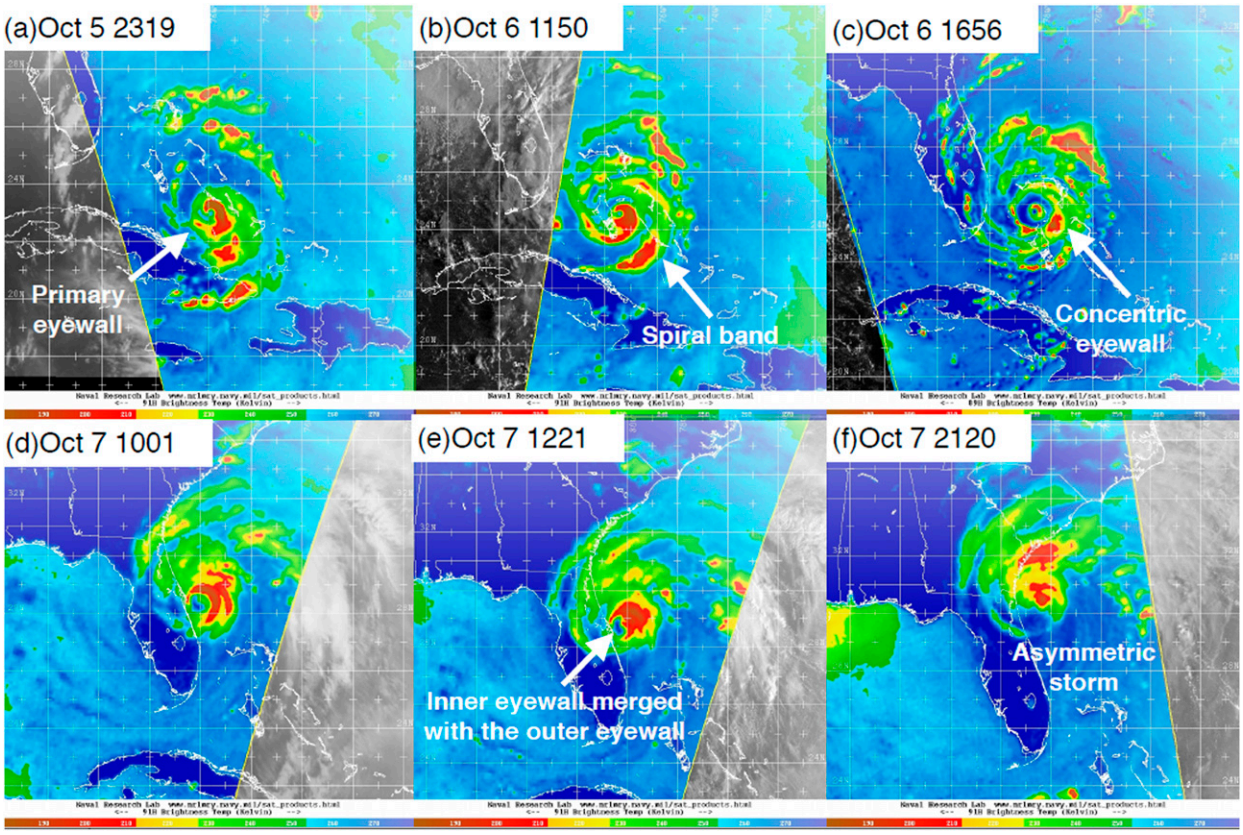

FIG. 4. The 89- and 91-GHz microwave satellite imagery of brightness temperatures at (a) 2319 UTC 5 Oct, (b) 1150 UTC 6 Oct, (c) 1656 UTC 6 Oct, (d)1001 UTC 7 Oct, (e) 1221 UTC 7 Oct, and (f) 2120 UTC 7 Oct, showing the convective evolution of Hurricane Matthew during ERC. Images are courtesy of the Naval Research Laboratory Monterey Tropical Cyclones web page.

The vertical velocity of the inner eyewall reached 3.3 m s^{-1} at 12.5-km altitude around 2100 UTC and the maximum tangential wind was up to 55.2 m s^{-1}, with a low-level radial inflow of 4.3 m s^{-1} (Fig. 6b). A distinct low-level tangential wind maximum (40 m s^{-1}) and a growing updraft up to 1 m s^{-1} in the mid- to upper levels appeared in the outer eyewall region. The secondary circulation of the secondary eyewall was vertically shallower compared to the primary eyewall, consistent with previous observations (Hence and Houze 2012; Bell et al. 2012b).

After 2200 UTC (Fig. 6c) the inner eyewall started to weaken, accompanied by a decaying radial gradient of tangential wind and a reduced secondary circulation. The low-level inflow over the inner eyewall region reduced to 3.1 m s^{-1}, and the updraft speed was only up to 1.2 m s^{-1}. The moat began to fill with precipitation with a descending flow outside of the inner eyewall. While the maximum tangential wind in the outer eyewall weakened slightly over this time period, the convection became more consolidated and continued to develop a stronger, independent secondary circulation (Fig. 6d). The low-level inflow over the outer eyewall region was up to 7.2 m s^{-1} and extended to 3-km altitude, and the low-level convergence increased at the leading edge of the strong inflow (not shown). The analysis suggests that the decaying inner eyewall was in response to lack of inflow due to the strong radial convergence at the outer eyewall. This "barrier effect," where the outer eyewall impedes the radial inflow into the inner eyewall, is consistent with previous observations of ERC evolution in Hurricane Rita (2005) (Bell et al. 2012b) and Hurricane Gonzalo (2014) (Didlake et al. 2017).

Figure 7 shows the azimuthally averaged absolute vorticity, angular momentum, and kinematic structure evolution. The absolute vorticity field at 1900 UTC (Fig. 7a) shows an upright vorticity tower located along the inner edge of the inner eyewall (Fig. 6a, reflectivity). The strong radial gradient of vorticity suggests that the moat region was associated with weak vorticity bounded by the enhanced vorticity of the two eyewalls. The maximum vorticity in the outer eyewall region was around 2-km altitude (between 40- and 60-km radius), but the value was much weaker compared to the vorticity in the inner eyewall (exceeding 8×10^{-3} s^{-1}).

As the vorticity of inner eyewall decayed and the 35 m s^{-1} tangential wind field expanded to the radius of 50–70 km and extended to the altitude of 5 km, the radial gradient of vorticity decreased over the four aircraft passes (Figs. 7a–d). The inner eyewall decreased from up to 9.3×10^{-3} s^{-1} in pass 1 to 7.4×10^{-3} s^{-1} in pass 4. In the outer eyewall, the vorticity increased in the lower levels, and was up to 1.4×10^{-3} s^{-1} extended to

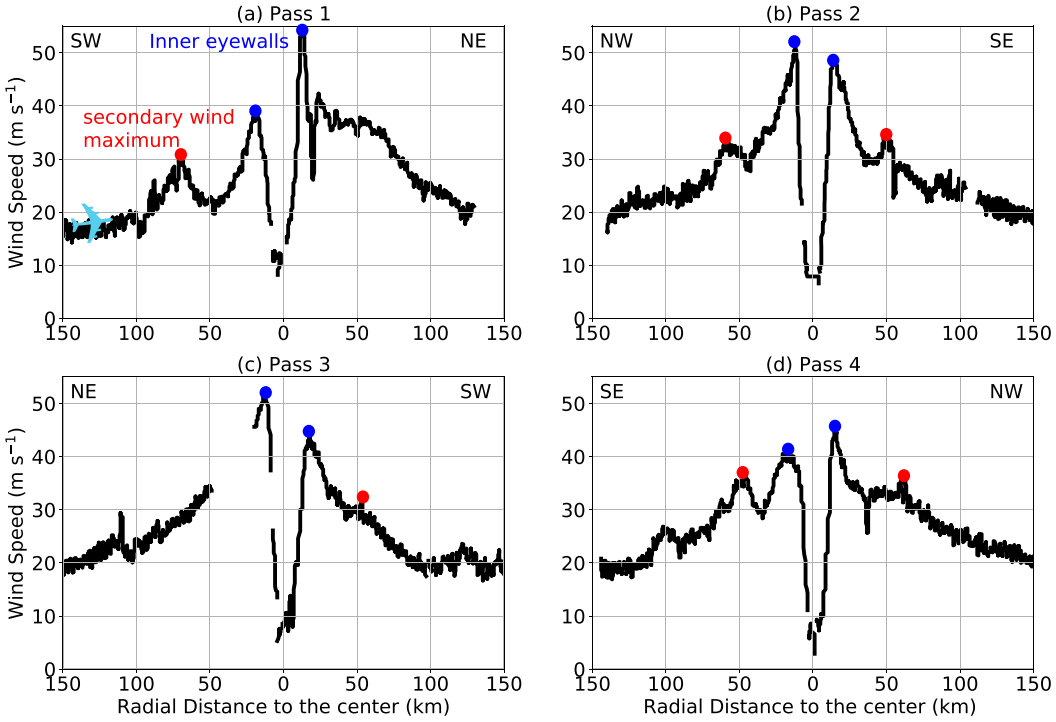

FIG. 5. The storm-centered surface wind derived from the P3 SFMR observations from 1900 UTC 6 Oct to 0000 UTC 7 Oct corresponding to four flight passes in Fig. 1. Light blue aircraft denotes the P–3 flight direction, and the direction of the track is noted on the top-left and top-right corners of each panel. The blue dots denote the primary wind maxima, and the red dots denote the secondary wind maxima.

4-km altitude by 2300 UTC (Fig. 7d) associated with more closely packed angular momentum surfaces that have an enhanced radial gradient, with a similar structure to that observed in Hurricane Rita (2005) (Bell et al. 2012b). The 1.2–2.1 $\times$ $10^6\,m^2\,s^{-1}$ surfaces moved radially inward at low levels over the analysis period as the tangential wind field expanded (Fig. 6d). As mentioned above, low-level convergence associated with a strong, deep inflow layer in the outer eyewall region (between 40 and 60 km) is found in pass 4. The intensification is consistent with the proposed axisymmetric intensification mechanism where increasing low-level inflow above the boundary layer leads to the convergence of angular momentum (Ooyama 1969; Shapiro and Willoughby 1982; Smith et al. 2009). We note that the radar analysis is likely underestimating the low-level inflow below 1 km due to missing data from sea clutter, and cannot reliably assess the second mechanism of radial convergence of angular momentum within the boundary layer proposed by Smith et al. (2009) from the observations. The axisymmetric structural evolution derived from the radar observations is consistent with an ongoing ERC process.

Triple-Doppler analyses from the four aircraft passes combined with the ground-based radar observations have shown the detailed convective and kinematic structure and evolution during the weakening stage of an ERC. The analysis points out several important features in the context of an ERC process. First, the analysis suggests that the decay of the inner eyewall was due to the barrier effect as the low-level convergence and radial inflow increased at the outer eyewall as it matured. Second, the increasing low-level convergence and inflow were associated with the expansion of tangential wind and increased vorticity near the base of the outer eyewall. Third, the moat signature disappeared and filled with precipitation as the secondary circulation of the inner eyewall weakened and the outer eyewall developed its own independent secondary circulation.

b. *Single-Doppler analysis*

The single-Doppler analysis period spans from 1900 UTC 6 October to 0000 UTC 8 October, using the KAMX, KMLB, and KJAX observations. During this period, the intensity of Matthew steadily dropped from category 4 to category 3, and the environmental shear amplitude increased from 4 to 14 m s^{-1}. Figures 8a–d displays the plan view of reflectivity evolution at a constant altitude, and Figs. 8e–h shows the corresponding vertical cross sections of the wavenumber-0 tangential wind. At 1930 UTC 6 October (Figs. 8a and 8e), the developing outer eyewall was roughly 70 km away from the eye, while the inner eyewall was associated with a nearly circular ring of convection where the strongest reflectivity was located in the downshear-left quadrant whereas the reflectivity maximum of the outer eyewall was located in the upshear left, consistent with the observations in Hence and Houze (2012) and Didlake et al. (2017). The radar loop of reflectivity evolution (not shown) indicates that the new cells periodically formed in the downshear-right quadrant, and the cells

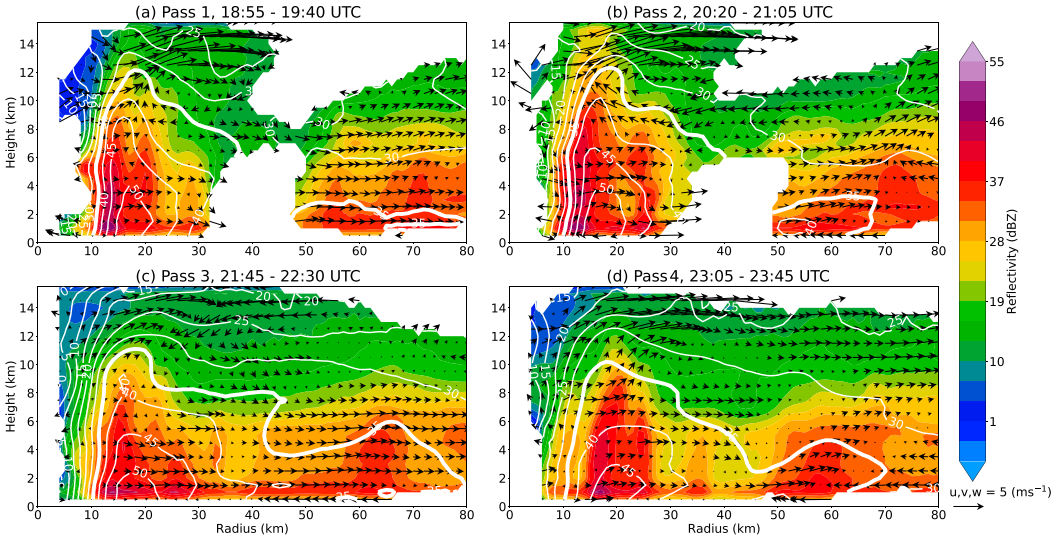

FIG. 6. Azimuthally averaged reflectivity (shaded), primary circulation (white contours, m s^{-1}), and secondary circulation (vectors) derived from the triple-Doppler analysis. Thick white contour highlights the azimuthally averaged tangential wind of 35 m s^{-1}. (a) Pass 1 (1855–1940 UTC), (b) pass 2 (2020–2105 UTC), (c) pass 3 (2145–2230 UTC), and (d) pass 4 (2305–2345 UTC).

dissipated in the upshear-left quadrant, consistent with previous observations (Reasor et al. 2009). The moat was largely convection free, which was bounded by the deep convection of the inner eyewall and developing outer eyewall. The axisymmetric tangential wind derived from the single-Doppler analysis generally resembled the azimuthally averaged tangential wind in pass 1 of the triple-Doppler analysis, associated with the intense primary circulation in the inner eyewall region and the signature of a developing outer eyewall.

By 0729 UTC 7 October, the maximum reflectivity in the inner eyewall decreased, and the inner eyewall became asymmetric and weak (Fig. 8b). The reflectivity maximum of both relict eyewall and outer eyewall were concentrated in the northeast quadrant, suggesting that VWS played an important role in modulating the storm's structure. Figure 8f shows that the axisymmetric primary circulation of the inner eyewall decayed and extended up to 3-km altitude only, while the axisymmetric primary circulation of the outer eyewall was over 50 m s^{-1}, associated with a broad tangential wind field from the radius of 40–60 km.

When the relict inner eyewall merged with the contracting outer eyewall (from 1300 to 1400 UTC 7 October), the radius

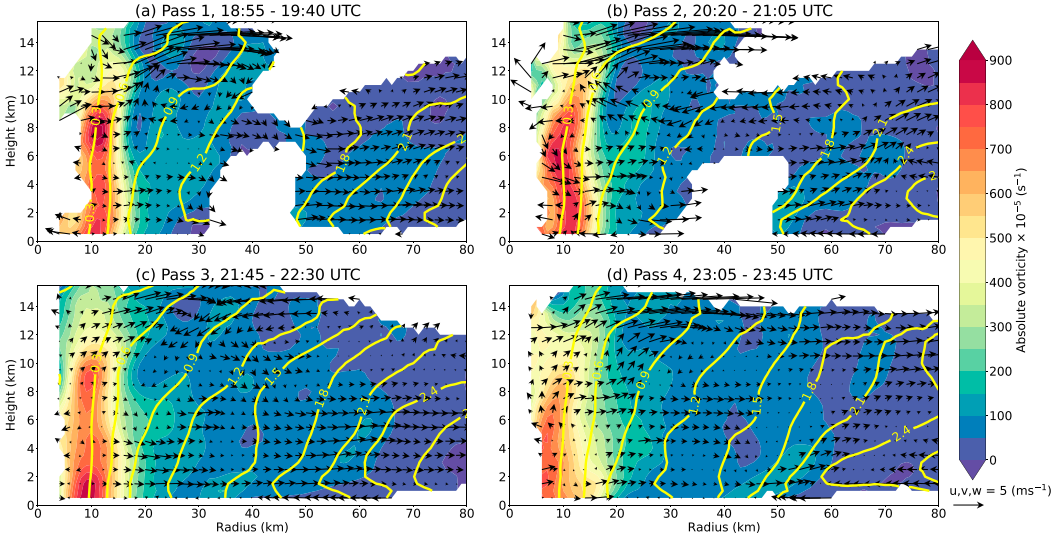

FIG. 7. Azimuthally averaged absolute vorticity (shaded, 10^{-5} s^{-1}), absolute angular momentum (yellow contours, 10^{-6} m^2 s^{-1}), and secondary circulation (vectors) derived from the triple-Doppler analysis. (a) Pass 1 (1855–1940 UTC), (b) pass 2 (2020–2105 UTC), (c) pass 3 (2145–2230 UTC), and (d) pass 4 (2305–2345 UTC).

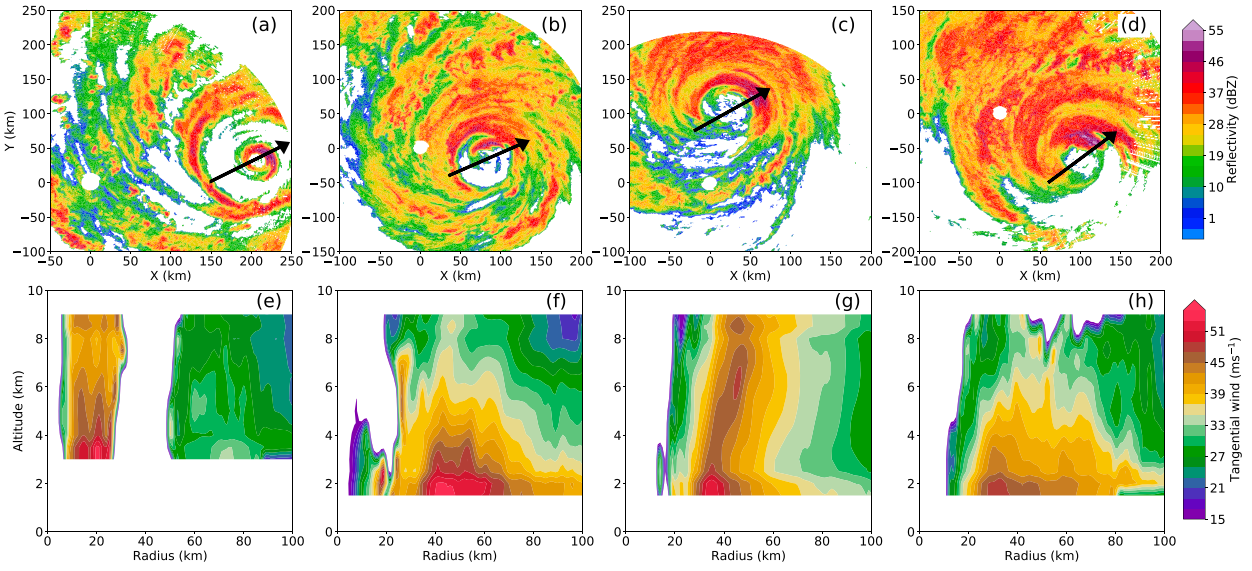

FIG. 8. (a)–(d) Plan view of reflectivity derived from KAMX radar at 1930 UTC 6 Oct at 4 km, KMLB radar at 0729 UTC 7 Oct at 3 km, KMLB radar at 1400 UTC 7 Oct at 3 km, and KJAX radar at 2126 UTC 7 Oct at 3 km, respectively. The black arrow denotes the environmental VWS direction from the SHIPS database. (e)–(h) Cross section of wavenumber-0 tangential wind derived from single-Doppler analysis at the same times and radars from (a) to (d), respectively.

of the eye expanded to ~38 km and the convection evolved into a semicircle concentrated on the downshear quadrant. The wavenumber-0 tangential wind evolved into a slightly tilted tower extending to the altitude of 9 km with over 45 m s^{-1} (Figs. 8c and 8g). Figures 8d and 8h show that the new eyewall continued contracting to the radius of 30 km but the tangential wind tower decayed and broadened. Although Matthew's intensity was weakening throughout the analysis period (Fig. 2), Matthew remained a major hurricane above category 3 intensity during this time.

Changes in convective and kinematic structure have been one of the most prominent indicators of eyewall replacement. Figure 9 shows the shear evolution, and wavenumber-0 reflectivity, tangential wind, and absolute vorticity temporal evolution at the altitude of 3 km. The wavenumber-0 reflectivity intensity of the inner eyewall gradually weakened, and vanished at 0630 UTC 7 October after the maximum tangential wind was taken over by the outer eyewall (Guimond et al. 2020), where the RMW increased with a jump from 20 to 52 km at 0330 UTC 7 October. The moat region was located between 30 and 50 km originally, but diminished after 2200 UTC, which is consistent with the triple-Doppler analysis. The outer eyewall contracted over the analysis period from a radius of 70 km at 1930 UTC 6 October to 40 km at 1530 UTC 7 October. The contraction rate of the outer eyewall is 1.5 km h^{-1}, which is similar to the composite value of 1.75 km h^{-1} in Sitkowski et al. (2011). We note that the wavenumber-0 reflectivity component of the outer eyewall decayed from 1030 to 1230 UTC 7 October, and reintensified hereafter as the inner eyewall merged with the outer eyewall, suggesting that the outer eyewall may have axisymmetrized the asymmetric relict inner eyewall.

Comparing Fig. 9a to Fig. 9c, the analysis shows that the intensification of the mean tangential wind of the outer eyewall was accompanied with a weakening intensity of the mean reflectivity. The radial broadening of tangential wind of the outer eyewall in Matthew was captured as the moat disappeared, which is consistent with the triple-Doppler analysis. The wavenumber-0 tangential wind in the outer eyewall gradually contracted with some fluctuations in intensity, and reached a maximum value (55 m s^{-1}) when the inner eyewall merged with the outer eyewall (1230–1400 UTC 7 October), and then decayed, similar to the axisymmetric reflectivity evolution.

Broadening of the tangential wind field is one of the common features associated with an ERC event. The tangential wind in the outer eyewall region above 40 m s^{-1} extended from the radius of 30 to 70 km after 0430 UTC 7 October, indicating that the area of damaging winds grew in size. To quantify the effect of the expansion of tangential wind, integrating the axisymmetric tangential wind component of kinetic energy $\int_0^{125}[\rho(v^2)/2]dr$ from the center to 125-km radius at the altitude of 3 km indicates that the integrated kinetic energy increased 21% from 2030 UTC 6 October to 0830 UTC 7 October. Despite the decay of intensity during this time, Matthew increased in size, resulting in a larger damage swath. After the inner eyewall disappeared, Matthew continued weakening while remaining close proximity to the coastline, suggesting that a combination of shear, land interaction, and unfavorable environment may have disrupted the reintensification phase and resulted in an asymmetric wind field. Figure 9d shows that the innermost vorticity maximum exceeded 9×10^{-3} s^{-1} in the beginning of the analysis period, and the vorticity profile across the eye and eyewall became broader and flatter after the outer wind maximum surpassed the inner wind maximum. The outermost vorticity maximum in the secondary eyewall region near the radius of 60 km emerged at 1930 UTC, located near the

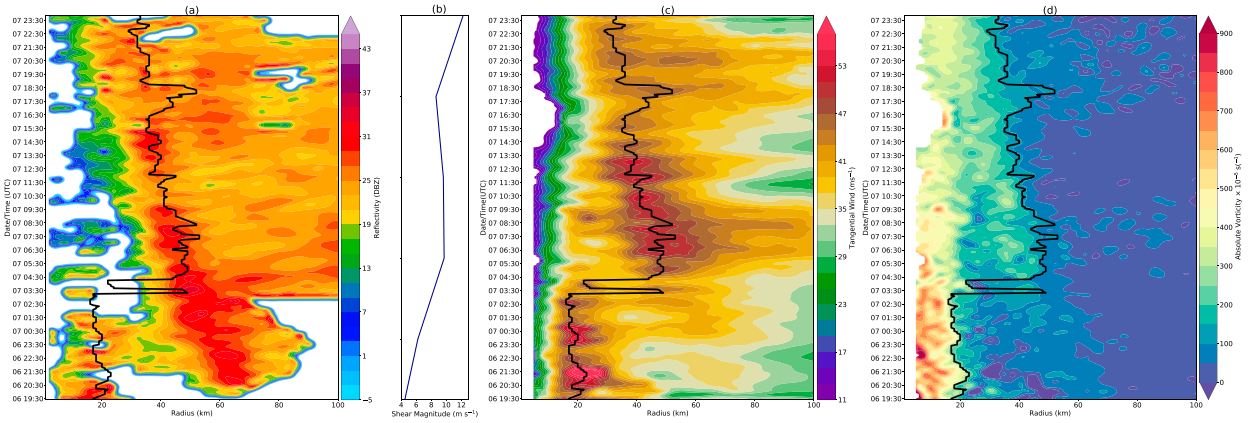

FIG. 9. Time–radius diagram of axisymmetric (a) reflectivity, (c) tangential wind, and (d) absolute vertical vorticity derived from the KAMX, KMLB, and KJAX radars at an altitude of 3 km from 1930 UTC 6 Oct to 0000 UTC 8 Oct. The black line denotes the RMW. (b) Interpolated shear amplitude derived from the SHIPS database.

inner edge of axisymmetric tangential wind. The RMW continued contracting and roughly followed the radial gradient of vorticity, while the reverse radial vorticity gradient between the inner and outer eyewalls diminished. Near the end of the analysis period, the innermost vorticity maximum was less than $5 \times 10^{-3}\,s^{-1}$, and was associated with the weakening axisymmetric components of tangential wind and reflectivity.

5. Asymmetric structure

a. Wavenumber-1 evolution

The evolutions of wavenumber-1 reflectivity and tangential wind fields at the altitude of 3 km are shown in Figs. 10a and 10c, with the corresponding shear amplitude shown in Fig. 10b. From 1930 UTC 6 October to 0330 UTC 7 October, the maximum amplitude of wavenumber-1 reflectivity in the inner eyewall was over 20 dBZ, which contributed to a large fraction of the total reflectivity field. Weaker wavenumber-1 components in both reflectivity (>10 dBZ) and tangential wind ($>5\,m\,s^{-1}$) fields are evident in the outer eyewall region. During this same period, the southwesterly environmental shear magnitude increased from 4 to $10\,m\,s^{-1}$. After the outer wind maximum exceeded the inner wind maximum (0330 UTC 7 October), the outer eyewall reflectivity pattern gradually evolved into an open circle (Fig. 8b). The increased shear magnitude suggests that the shear became more influential on the outer eyewall asymmetry than the earlier period.

By 0430 UTC 7 October, the wavenumber-1 reflectivity strengthed gradually, while the wavenumber-1 tangential wind started to increase episodically (Guimond et al. 2020) with a peak value of 10–12 $m\,s^{-1}$ and continued contracting for the next 16 h. The shear amplitude was moderate between 9 and 11 $m\,s^{-1}$ at this time. In Reasor et al. (2004), they proposed a conceptual model for the resiliency of a vortex impacted by the vertical shear flow. Although this conceptual model has not been discussed or observed in an ERC process before to the authors' knowledge, the episodic increases of wavenumber-1 tangential wind of the outer eyewall in here are hypothesized to be a result of the interaction between the shear and the vortex. Therefore, we will mainly focus on the outer eyewall region in the upcoming discussion.

To track the outer eyewall azimuthal evolution, Fig. 11 shows the azimuthal distribution of wavenumber-1 averaged over the radial bands between RMW − 2 km and RMW + 2 km from 0630 to 2330 UTC 7 October. The shear was moderate at about $10\,m\,s^{-1}$ and increased to $14\,m\,s^{-1}$ near the end of the analysis period, with a slight shift in direction from southwesterly to southerly. The wavenumber-1 reflectivity initially resided in the upshear-left quadrant and rotated to the downshear-left quadrant, consistent with the result of azimuthal upwind shift for the reflectivity from Didlake et al. (2017). Although Didlake et al. (2017) did not show the azimuthal distribution of tangential wind, Fig. 11b illustrates that wavenumber-1 tangential wind rotated to downshear-left (DL) quadrant along with the reflectivity, and the wavenumber-1 reflectivity stayed left of shear for the rest of the period while the tangential wind continued rotating cyclonically and mostly stayed downshear right (DR).

Different maximum quadrants of reflectivity (DL) and tangential wind (DR) suggests the contributions of both external and internal forcings. Although Matthew did not make landfall during our analysis period, the outer eyewall was circulating near the coast and the storm would receive impacts from the land, such as dry air intrusion and surface friction. As the primary circulation spun cyclonically, the tangential wind would slow down on the west side (upshear) due to the land friction. Moreover, the drier air from the land and relatively low sea surface temperature (SST) as Matthew continued a northward track may have also modified the convective and kinematic structure distribution. Hence, we hypothesize that the combination of the internal vortex dynamics, environmental properties, land interaction, and shear direction may have played a role in the azimuthal distribution of wavenumber-1 reflectivity and tangential wind.

When the outer eyewall replaced the inner eyewall (0600–1800 UTC 7 October), the deep-layer environmental vertical shear was about 9–11 $m\,s^{-1}$ with a slight reduction of amplitude between 1200 and 1800 UTC 7 October, while the

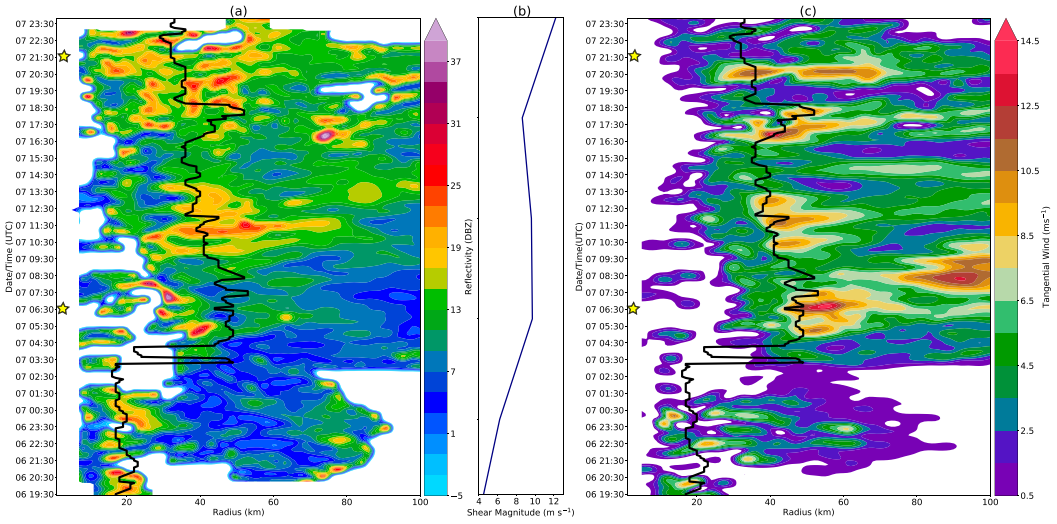

FIG. 10. Time–radius diagram of wavenumber-1 (a) reflectivity and (c) tangential wind from the KAMX, KMLB, and KJAX radars at an altitude of 3 km from 1930 UTC 6 Oct to 0000 UTC 8 Oct. The black line denotes the RMW. (b) Interpolated shear amplitude derived from the SHIPS database.

wavenumber-1 reflectivity and tangential wind components both increased. Guimond et al. (2020) shows that the convectively coupled VRWs were active in the radial distance from 75 to 125 km from the center during this time. VRW activity is examined in more detail in the following section.

b. *Wavenumber-2 evolution*

The radar images (Figs. 8b and 8c) have shown that Matthew's outer eyewall exhibited noncircular shapes. Previous studies have shown the linkage of noncircular eyewall shapes to vortex Rossby waves dynamics (Kuo et al. 1999; Corbosiero et al. 2006; Cha et al. 2020). The propagation of a VRW can transport momentum radially along the mean vorticity gradient. When a VRW interacts with a sheared vortex, the VRW damping mechanism can contribute to the vortex realignment process (Reasor et al. 2004). Figures 12a and 12c show the wavenumber-2 azimuthal evolution of reflectivity and tangential wind tracked by the RMW and averaged over 5 km radial bands, and Fig. 12b shows the corresponding shear amplitude evolution. Both wavenumber-2 tangential and reflectivity components stayed in the same quadrant between 0630 and 0730 UTC 7 October. The positive wavenumber-2 component of the tangential wind and the reflectivity from 0730 to 1130 UTC completed four full azimuthal rotations, and the wavenumber-2 component of the tangential wind continued rotating cyclonically while the wavenumber-2 reflectivity mostly stayed in the same quadrant for the rest of time.

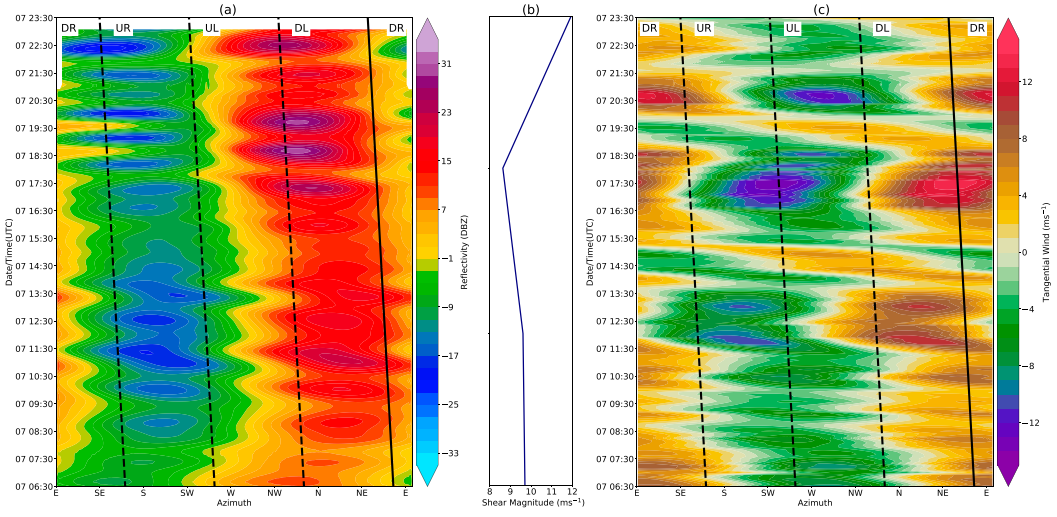

FIG. 11. Time–azimuth diagram of wavenumber-1 (a) reflectivity and (c) tangential wind averaged between RMW − 2 km and RMW + 2 km from the center of Matthew with the KMLB and KJAX radars at the altitude of 3 km from 0630 to 2330 UTC 7 Oct. Thick black line denotes the shear direction interpolated from the SHIPS database. (b) Interpolated shear amplitude derived from the SHIPS database.

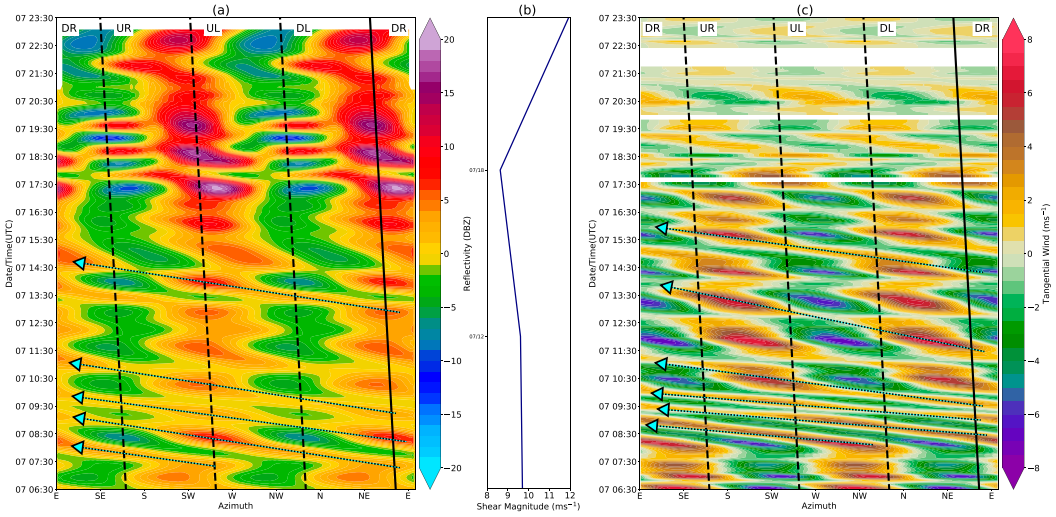

FIG. 12. Time–azimuth diagram of wavenumber-2 (a) reflectivity and (c) tangential wind averaged between RMW − 2 km and RMW + 2 km from the center of Matthew with the KMLB and KJAX radars at the altitude of 3 km from 0430 to 2200 UTC 7 Oct. The thick black line denotes the shear direction interpolated from the SHIPS database. (b) Interpolated shear amplitude derived from the SHIPS database. The black arrow with cyan head highlights the propagation of the wavenumber-2 features.

A power spectrum analysis in the frequency domain following the method in Cha et al. (2020) was performed, and the estimated azimuthal phase speed of the wavenumber-2 tangential wind bands was 29.76 m s^{-1} at approximately a radius of 42 km from 0630 to 1730 UTC. Linear VRW theory indicates that the azimuthal propagation speed is $C_\lambda = V_{\max}(1 - 1/n)$, where $V_{\max}$ is the maximum tangential speed of the mean flow, and n is the azimuthal tangential wavenumber (Lamb 1932; Guinn and Schubert 1993). The theoretical wavenumber-2 rotation rate will therefore be nearly half of the maximum tangential speed (Kuo et al. 1999). The retrieved phase speed is about 58% of the maximum tangential speed of the mean flow, consistent with the linear wave theory. Guimond et al. (2020) also shows the evidence of VRWs from the radial distance of 50 to 125 km with HIWRAP observations between 1- and 1.5-km altitude under the similar period. Their estimated azimuthal phase speed of the bands is 24.5 m s^{-1} at the radius of 50 km. The discrepancy between the two estimations can be attributed to the different choice of radius (42 vs 50 km) and altitude (3 vs 1–1.5 km). The consistent analysis suggests that the observed asymmetries can be well explained by the VRW dynamics. The cyclonic propagation of the wavenumber-2 tangential wind was prominent between 0830 and 1730 UTC 7 October, while the wavenumber-1 tangential wind slightly weakened between 1330 and 1530 UTC and reintensified afterward when the shear started to increase.

As the shear increased rapidly near the end of observation, the storm was clearly dominated by the wavenumber-1 component (Figs. 8c and 8d). The propagation of wavenumber-2 tangential wind component weakened and stayed in the same quadrant during the intensifying shear, and the magnitude became smaller in the tangential wind field but stronger in the reflectivity field. This inverse behavior of the wavenumber-2 reflectivity and tangential wind is uncertain, but one possibility could be due to the limitations of the GVTD retrieval method. While the partition between the tangential and radial wind is uncertain, the Doppler analysis does constrain the total amplitude of the wavenumber-2 component, suggesting that there was a physical decrease in this component of the wind asymmetry despite the stronger reflectivity amplitude. A cross-spectrum analysis between the wavenumber-2 reflectivity and tangential wind from 0630 to 1730 UTC is performed, and a phase difference of 12° is found between the two. We speculate that the reflectivity and vorticity may not be fully coupled under the stronger shear, consistent with the modeling study of Moon and Nolan (2015).

To examine the vortex realignment process, the GVTD-simplex centers evolution derived from the KMLB and KJAX radar observations are shown in Fig. 13. Each level is symbol-coded, and the corresponding shear is shown by the black arrow. Centers at different levels oscillated and circulated around each other during the period where the propagation of wavenumber-2 tangential winds were prominent from 0700 to 1000 UTC 7 October. At 1309 UTC, the vertical centers became more aligned and less than 5 km apart, suggesting the reduction of the vortex tilt and corresponding to a weakening wavenumber-1 tangential wind (Fig. 10c) and a strengthening wavenumber-0 tangential wind (Fig. 9c), despite the strong environmental shear of 9 m s^{-1}. An hour later, the vertical centers started to diverge, and never fully realigned. The centers at upper levels were generally in the downshear quadrant, whereas the centers at lower levels were generally in the upshear quadrant as the shear intensified.

To facilitate the illustration, Fig. 14 presents plan views of the TC inner core reflectivity centered on the dynamic centers at 3-km altitude. At 0837 UTC, the GVTD-simplex centers at 1-, 3-, and 7-km altitude were less than 10 km away from the dynamic center but scattered along the NW to SE direction, whereas the centers at 5- and 9-km altitude were at a radial distance of ~20 km and were southwest of the dynamic center.

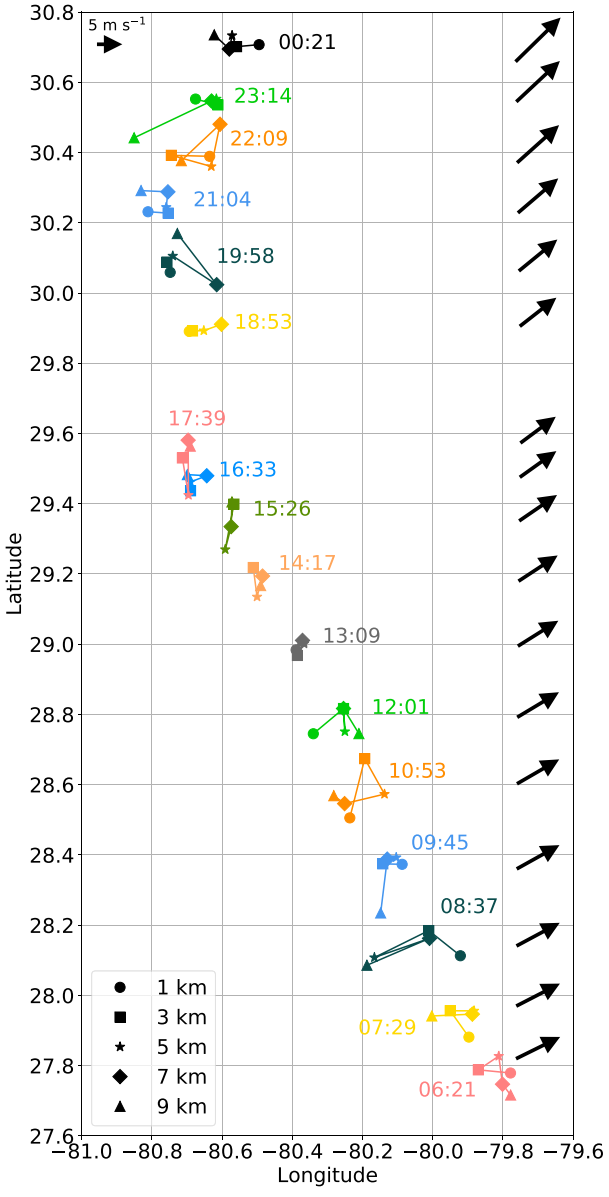

FIG. 13. GVTD-simplex centers at 1-, 3-, 5-, 7-, and 9-km altitude from 0621 UTC 7 Oct to 0021 UTC 8 Oct. The length and direction of black arrows represent the shear amplitude and shear direction interpolated from the SHIPS database. Each arrow corresponds to the times of the GVTD-simplex center analysis.

At 1309 UTC, the GVTD-simplex centers were vertically aligned less than 3 km apart from each other, and were very consistent with the dynamic center. At 2209 UTC, the reflectivity was more asymmetric, and the GVTD-simplex centers at different levels diverged from the dynamic center at 3-km altitude by up to 15 km. Although there is some uncertainty in the GVTD-simplex centers on the order of 1–3 km (Cha and Bell 2021), the single-Doppler derived centers provide qualitative and quantitative evidence for the resilient eyewall and the vortex realignment process, and are generally consistent with the evolution of the vortex asymmetries.

A composite study of the ERC storms from Sitkowski et al. (2011) shows an average of 2 m s^{-1} increase in the maximum wind of the outer eyewall in the reintensification phase. Unlike a canonical ERC, the reintensification phase was never realized due to the increasing shear and an unfavorable environment. However, Matthew did not rapidly weaken despite the shear, and the analyses herein present evidence that suggests the vortex resiliency conceptual model from Reasor et al. (2004) may be applicable to Matthew's outer eyewall evolution. Due to limitations of the dataset we cannot quantitatively assess the impact of VRWs on the resiliency and realignment process, but hypothesize that the VRW damping mechanism may play an important role in the ERC process impacted by the shear. Furthermore, Guimond et al. (2020) demonstrates the VRW activity in the boundary layer in support of the secondary eyewall formation around the same time as our findings of the realignment process, which further supports our hypothesis.

6. Conclusions

The structure and evolution of Hurricane Matthew were examined using the triple-Doppler and single-Doppler analysis, supporting previous studies of the eyewall replacement cycle (ERC) in an axisymmetric framework and providing new insights into the asymmetric evolution during an ERC. The high spatial resolution of the triple-Doppler analysis complements the lower spatial resolution of the single-Doppler analysis, with the single-Doppler analysis providing high temporal resolution during the whole ERC process in detail. Four passes of the triple-Doppler analysis show detailed convective and kinematic evolution of a weakening inner eyewall and a developing outer eyewall. The weakening inner eyewall was associated with a decaying secondary circulation as the clear moat region filled in over time, while the strengthening outer eyewall was accompanied by an increasing secondary circulation and a broadening of tangential wind field. The vertical vorticity of the developing outer eyewall was maximized at low levels and closely coupled with low-level inflow and convergence of angular momentum. The development of the outer eyewall supports the axisymmetric intensification mechanism proposed by Ooyama (1969), Shapiro and Willoughby (1982), and Smith et al. (2009) as a well-recognized framework for understanding intensification, but uniquely applied to the secondary instead of primary eyewall.

A total of 35 h of the single-Doppler analysis documents the dissipation of the inner eyewall and contraction of the outer eyewall with increasing asymmetry due to increasing vertical wind shear (VWS). The analysis suggests Matthew's ERC evolution is consistent with intensification and weakening stages of a classic ERC (Sitkowski et al. 2011), but reintensification was never realized due to increasing VWS. The beginning of the observation period shows that the clear moat and concentric eyewall pattern were distinct, suggesting that the secondary circulation of the inner eyewall was still intense. The asymmetries of the inner eyewall increased gradually as the shear increased and the inner eyewall merged with the outer eyewall in the later period. When the shear magnitude intensified to around 9–11 m s^{-1}, the asymmetries of the outer eyewall increased episodically, suggesting the vortex was able

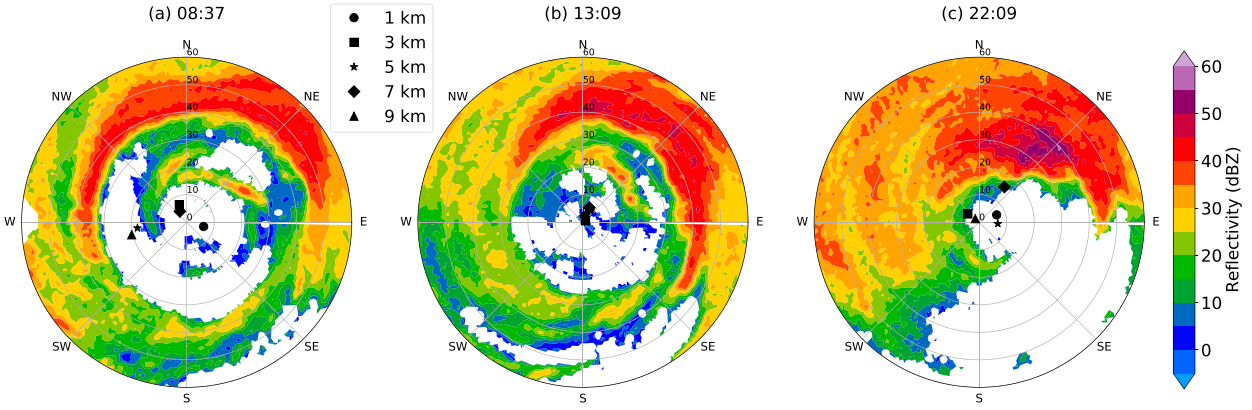

FIG. 14. Plan view of reflectivity centered on the aircraft-derived dynamic centers at altitude derived from the KMLB radar at (a) 0837 and (b) 1309 UTC, and from the KJAX radar at (c) 2209 UTC. The GVTD-simplex centers at 1-, 3-, 5-, 7-, and 9-km altitude are symbol coded. The interval of concentric circles is 10 km.

to damp the asymmetries and be resilient to the VWS. Furthermore, the derived wavenumber-2 tangential wind field shows evidence of propagating vortex Rossby waves (VRWs) in the outer eyewall region that suggests internal asymmetric dynamics played an important role in the ERC evolution. Our results are not inconsistent with that interpretation with the findings of Guimond et al. (2020) that VRWs spawned by the outer eyewall may have played an important role in the development of a ''secondary'' outer eyewall. Here we further argue that the VRW activity associated with the outer eyewall after the decay of the inner eyewall was important to maintain the vortex resiliency in spite of the increasing VWS, consistent with the VRW damping mechanism proposed by Reasor et al. (2004). At the end of analysis period when the shear continued to increase beyond 11 m s^{-1}, the asymmetric structure of Matthew was dominated by the shear, and the VRW propagation weakened. At that time, the wavenumber-2 reflectivity field was not consistent with the retrieved tangential wind field, suggesting that the asymmetric vorticity and reflectivity were no longer coupled (cf. Moon and Nolan 2015).

Figure 15 presents a novel simplified 3D schematic of the inner and outer eyewall vorticity tower evolution to summarize Matthew's ERC. The GVTD-simplex centers (white line) show the vortex tilt, and the retrieved axisymmetric vertical

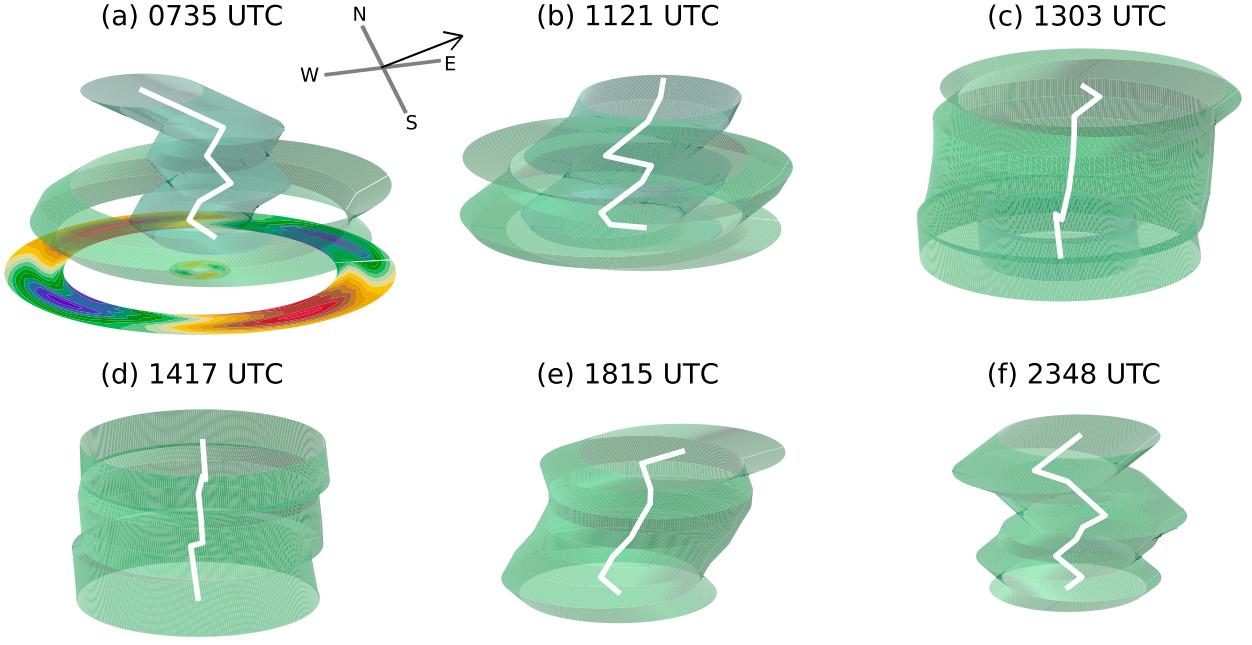

FIG. 15. 3D simplified plots of Matthew's inner and outer vorticity tower evolution at (a) 0735, (b) 1121, (c) 1303, (d) 1417, (e) 1815, and (f) 2348 UTC 7 Oct. The white line denotes the GVTD-simplex centers at different altitudes, and the inner and outer radii of vorticity towers were estimated from the axisymmetric vorticity profile. The black arrow represents the environmental shear direction. Shading at 0735 UTC shows the wavenumber-2 tangential wind at $z = 3$ km.

vorticity is schematically depicted to indicate the depth and radius of the inner and outer eyewalls. From 0735 to 1121 UTC, the outer eyewall vorticity intensified and increased in depth while the inner eyewall vorticity weakened but was still intense. The vortex centers were not vertically aligned as the TC was impacted by shear and vortex precession. A cyclonic propagation of the wavenumber-2 tangential wind in the outer eyewall region during this period was prominent and is indicated by the color shading. The inner eyewall continued to weaken at 1303 UTC, and dissipated by 1417 UTC, while the outer eyewall continued to strengthen and the vortex became vertically aligned. By 1815 UTC, the upper-level centers became displaced to the northeast relative to the lower-levels centers to the southwest, as the vortex tilt became aligned with the shear direction. As the shear continued to intensify, the vortex continued to contract but never fully realigned in the vertical and Matthew's intensity continued to decay.

We summarize briefly the key points of this study as follows:

- Matthew's ERC process was a complex combination of both internal axisymmetric and asymmetric dynamics that were impacted by external factors of environmental shear and land interaction.
- The canonical ERC process can be interrupted by strong shear, and in Matthew's case was not able to enter the reintensification stage found in other ERCs.
- The reduction of vortex tilt despite increasing shear and presence of VRW activity suggests that the VRW damping mechanism and vortex resiliency conceptual model proposed by Reasor et al. (2004) may be applicable to the ERC process.

While the radar observations analyzed here provide valuable new insights into Matthew's ERC process, continued research on the VRW damping mechanism and vortex resiliency in shear using numerical modeling is recommended. Additional complexities from the nearby land interactions and internal dynamics of the evolving axisymmetric and asymmetric secondary circulation also require further study and will be the subject of future work.

Acknowledgments. This research was supported by National Science Foundation Award OAC-1661663 and Office of Naval Research Awards N000141613033 and N000142012069. T.-Y. Cha was also supported by a Taiwan Ministry of Education graduate fellowship. We thank NOAA Aircraft Operations Center and the Hurricane Research Division of the Atlantic Oceanographic and Meteorological Laboratory for collecting the airborne tail Doppler radar data used for this study, and the National Weather Service for the ground-based radar data. We thank three anonymous reviewers for constructive and helpful comments.

REFERENCES

Bell, M. M., 2019: nsf-lrose/lrose-blaze: lrose-blaze-20190105. Accessed 6 January 2019, https://doi.org/10.5281/zenodo.2532758.

——, M. T. Montgomery, and K. A. Emanuel, 2012a: Air–sea enthalpy and momentum exchange at major hurricane wind speeds observed during CBLAST. *J. Atmos. Sci.*, **69**, 3197–3222, https://doi.org/10.1175/JAS-D-11-0276.1.

——, ——, and W.-C. Lee, 2012b: An axisymmetric view of concentric eyewall evolution in Hurricane Rita (2005). *J. Atmos. Sci.*, **69**, 2414–2432, https://doi.org/10.1175/JAS-D-11-0167.1.

——, W.-C. Lee, C. A. Wolff, and H. Cai, 2013: A solo-based automated quality control algorithm for airborne tail Doppler radar data. *J. Appl. Meteor. Climatol.*, **52**, 2509–2528, https://doi.org/10.1175/JAMC-D-12-0283.1.

Black, M. L., and H. E. Willoughby, 1992: The concentric eyewall cycle of Hurricane Gilbert. *Mon. Wea. Rev.*, **120**, 947–957, https://doi.org/10.1175/1520-0493(1992)120<0947:TCECOH>2.0.CO;2.

——, J. Gamache, F. Marks, C. Samsury, and H. Willoughby, 2002: Eastern Pacific Hurricanes Jimena of 1991 and Olivia of 1994: The effect of vertical shear on structure and intensity. *Mon. Wea. Rev.*, **130**, 2291–2312, https://doi.org/10.1175/1520-0493(2002)130<2291:EPHJOA>2.0.CO;2.

Boehm, A. M., and M. M. Bell, 2021: Retrieved thermodynamic structure of Hurricane Rita (2005) from airborne multi-Doppler radar data. *J. Atmos. Sci.*, **78**, 1583–1605, https://doi.org/10.1175/JAS-D-20-0195.1.

Cai, H., W.-C. Lee, M. M. Bell, C. A. Wolff, X. Tang, and F. Roux, 2018: A generalized navigation correction method for airborne Doppler radar data. *J. Atmos. Oceanic Technol.*, **35**, 1999–2017, https://doi.org/10.1175/JTECH-D-18-0028.1.

Cha, T.-Y., and M. M. Bell, 2021: Comparison of single-Doppler and multiple-Doppler wind retrievals in Hurricane Matthew (2016). *Atmos. Meas. Tech.*, **14**, 3523–3539, https://doi.org/10.5194/amt-14-3523-2021.

——, ——, W.-C. Lee, and A. J. DesRosiers, 2020: Polygonal eyewall asymmetries during the rapid intensification of Hurricane Michael (2018). *Geophys. Res. Lett.*, **47**, e2020GL087919, https://doi.org/10.1029/2020GL087919.

Corbosiero, K. L., and J. Molinari, 2003: The relationship between storm motion, vertical wind shear, and convective asymmetries in tropical cyclones. *J. Atmos. Sci.*, **60**, 366–376, https://doi.org/10.1175/1520-0469(2003)060<0366:TRBSMV>2.0.CO;2.

——, ——, A. R. Aiyyer, and M. L. Black, 2006: The structure and evolution of Hurricane Elena (1985). Part II: Convective asymmetries and evidence for vortex Rossby waves. *Mon. Wea. Rev.*, **134**, 3073–3091, https://doi.org/10.1175/MWR3250.1.

DeHart, J. C., R. A. Houze Jr., and R. F. Rogers, 2014: Quadrant distribution of tropical cyclone inner-core kinematics in relation to environmental shear. *J. Atmos. Sci.*, **71**, 2713–2732, https://doi.org/10.1175/JAS-D-13-0298.1.

DeMaria, M., M. Mainelli, L. K. Shay, J. A. Knaff, and J. Kaplan, 2005: Further improvements to the Statistical Hurricane Intensity Prediction Scheme (SHIPS). *Wea. Forecasting*, **20**, 531–543, https://doi.org/10.1175/WAF862.1.

Didlake, A. C., and R. A. Houze, 2011: Kinematics of the secondary eyewall observed in Hurricane Rita (2005). *J. Atmos. Sci.*, **68**, 1620–1636, https://doi.org/10.1175/2011JAS3715.1.

——, G. M. Heymsfield, P. D. Reasor, and S. R. Guimond, 2017: Concentric eyewall asymmetries in Hurricane Gonzalo (2014) observed by airborne radar. *Mon. Wea. Rev.*, **145**, 729–749, https://doi.org/10.1175/MWR-D-16-0175.1.

Foerster, A. M., and M. M. Bell, 2017: Thermodynamic retrieval in rapidly rotating vortices from multiple-Doppler radar data. *J. Atmos. Oceanic Technol.*, **34**, 2353–2374, https://doi.org/10.1175/JTECH-D-17-0073.1.

——, ——, P. A. Harr, and S. C. Jones, 2014: Observations of the eyewall structure of Typhoon Sinlaku (2008) during the transformation stage of extratropical transition. *Mon. Wea. Rev.*, **142**, 3372–3392, https://doi.org/10.1175/MWR-D-13-00313.1.

Guimond, S. R., J. A. Zhang, J. Sapp, and S. J. Frasier, 2018: Coherent turbulence in the boundary layer of Hurricane Rita (2005) during an eyewall replacement cycle. *J. Atmos. Sci.*, **75**, 3071–3093, https://doi.org/10.1175/JAS-D-17-0347.1.

——, P. D. Reasor, G. M. Heymsfield, and M. M. McLinden, 2020: The dynamics of vortex Rossby waves and secondary eyewall development in Hurricane Matthew (2016): New insights from radar measurements. *J. Atmos. Sci.*, **77**, 2349–2374, https://doi.org/10.1175/JAS-D-19-0284.1.

Guinn, T. A., and W. H. Schubert, 1993: Hurricane spiral bands. *J. Atmos. Sci.*, **50**, 3380–3403, https://doi.org/10.1175/1520-0469(1993)050<3380:HSB>2.0.CO;2.

Hence, D. A., and R. A. Houze, 2012: Vertical structure of tropical cyclones with concentric eyewalls as seen by the TRMM Precipitation Radar. *J. Atmos. Sci.*, **69**, 1021–1036, https://doi.org/10.1175/JAS-D-11-0119.1.

Hoose, H. M., and J. A. Colón, 1970: Some aspects of the radar structure of Hurricane Beulah on September 9, 1967. *Mon. Wea. Rev.*, **98**, 529–533, https://doi.org/10.1175/1520-0493(1970)098<0529:SAOTRS>2.3.CO;2.

Houze, R. A., S. S. Chen, B. F. Smull, W.-C. Lee, and M. M. Bell, 2007: Hurricane intensity and eyewall replacement. *Science*, **315**, 1235–1239, https://doi.org/10.1126/science.1135650.

Jones, S. C., 1995: The evolution of vortices in vertical shear. I: Initially barotropic vortices. *Quart. J. Roy. Meteor. Soc.*, **121**, 821–851, https://doi.org/10.1002/qj.49712152406.

Jou, B. J.-D., W.-C. Lee, S.-P. Liu, and Y.-C. Kao, 2008: Generalized VTD retrieval of atmospheric vortex kinematic structure. Part I: Formulation and error analysis. *Mon. Wea. Rev.*, **136**, 995–1012, https://doi.org/10.1175/2007MWR2116.1.

Kaplan, J., and M. DeMaria, 2003: Large-scale characteristics of rapidly intensifying tropical cyclones in the North Atlantic basin. *Wea. Forecasting*, **18**, 1093–1108, https://doi.org/10.1175/1520-0434(2003)018<1093:LCORIT>2.0.CO;2.

Koch, S. E., M. desJardins, and P. J. Kocin, 1983: An interactive Barnes objective map analysis scheme for use with satellite and conventional data. *J. Climate Appl. Meteor.*, **22**, 1487–1503, https://doi.org/10.1175/1520-0450(1983)022<1487:AIBOMA>2.0.CO;2.

Kuo, H.-C., R. Williams, and J.-H. Chen, 1999: A possible mechanism for the eye rotation of Typhoon Herb. *J. Atmos. Sci.*, **56**, 1659–1673, https://doi.org/10.1175/1520-0469(1999)056<1659:APMFTE>2.0.CO;2.

Lamb, H., 1932: *Hydrodynamics*. Cambridge University Press, 732 pp.

Laurencin, C. N., A. C. Didlake Jr., S. D. Loeffler, M. R. Kumjian, and G. M. Heymsfield, 2020: Hydrometeor size sorting in the asymmetric eyewall of Hurricane Matthew (2016). *J. Geophys. Res. Atmos.*, **125**, e2020JD032671, https://doi.org/10.1029/2020JD032671.

Lee, W.-C., B. J.-D. Jou, P.-L. Chang, and F. D. Marks, 2000: Tropical cyclone kinematic structure retrieved from single-Doppler radar observations. Part III: Evolution and structures of Typhoon Alex (1987). *Mon. Wea. Rev.*, **128**, 3982–4001, https://doi.org/10.1175/1520-0493(2000)129<3982:TCKSRF>2.0.CO;2.

Lorsolo, S., and A. Aksoy, 2012: Wavenumber analysis of azimuthally distributed data: Assessing maximum allowable gap size. *Mon. Wea. Rev.*, **140**, 1945–1956, https://doi.org/10.1175/MWR-D-11-00219.1.

Montgomery, M. T., and R. J. Kallenbach, 1997: A theory for vortex Rossby-waves and its application to spiral bands and intensity changes in hurricanes. *Quart. J. Roy. Meteor. Soc.*, **123**, 435–465, https://doi.org/10.1002/qj.49712353810.

Moon, Y., and D. S. Nolan, 2015: Spiral rainbands in a numerical simulation of Hurricane Bill (2009). Part II: Propagation of inner rainbands. *J. Atmos. Sci.*, **72**, 191–215, https://doi.org/10.1175/JAS-D-14-0056.1.

Ooyama, K. V., 1969: Numerical simulation of the life cycle of tropical cyclones. *J. Atmos. Sci.*, **26**, 3–40, https://doi.org/10.1175/1520-0469(1969)026<0003:NSOTLC>2.0.CO;2.

——, 1987: Scale-controlled objective analysis. *Mon. Wea. Rev.*, **115**, 2479–2506, https://doi.org/10.1175/1520-0493(1987)115<2479:SCOA>2.0.CO;2.

——, 2002: The cubic-spline transform method: Basic definitions and tests in a 1D single domain. *Mon. Wea. Rev.*, **130**, 2392–2415, https://doi.org/10.1175/1520-0493(2002)130<2392:TCSTMB>2.0.CO;2.

Qiu, X., Z.-M. Tan, and Q. Xiao, 2010: The roles of vortex Rossby waves in hurricane secondary eyewall formation. *Mon. Wea. Rev.*, **138**, 2092–2109, https://doi.org/10.1175/2010MWR3161.1.

Razin, M. N., and M. M. Bell, 2021: The unconventional eyewall replacement cycle of Hurricane Ophelia (2005). *Mon. Wea. Rev.*, **149**, 2151–2170, https://doi.org/10.1175/MWR-D-20-0181.1.

Reasor, P. D., and M. T. Montgomery, 2001: Three-dimensional alignment and corotation of weak, TC-like vortices via linear vortex Rossby waves. *J. Atmos. Sci.*, **58**, 2306–2330, https://doi.org/10.1175/1520-0469(2001)058<2306:TDAACO>2.0.CO;2.

——, and M. D. Eastin, 2012: Rapidly intensifying Hurricane Guillermo (1997). Part II: Resilience in shear. *Mon. Wea. Rev.*, **140**, 425–444, https://doi.org/10.1175/MWR-D-11-00080.1.

——, M. T. Montgomery, and L. D. Grasso, 2004: A new look at the problem of tropical cyclones in vertical shear flow: Vortex resiliency. *J. Atmos. Sci.*, **61**, 3–22, https://doi.org/10.1175/1520-0469(2004)061<0003:ANLATP>2.0.CO;2.

——, M. D. Eastin, and J. F. Gamache, 2009: Rapidly intensifying Hurricane Guillermo (1997). Part I: Low-wavenumber structure and evolution. *Mon. Wea. Rev.*, **137**, 603–631, https://doi.org/10.1175/2008MWR2487.1.

——, R. Rogers, and S. Lorsolo, 2013: Environmental flow impacts on tropical cyclone structure diagnosed from airborne Doppler radar composites. *Mon. Wea. Rev.*, **141**, 2949–2969, https://doi.org/10.1175/MWR-D-12-00334.1.

Rios-Berrios, R., and R. D. Torn, 2017: Climatological analysis of tropical cyclone intensity changes under moderate vertical wind shear. *Mon. Wea. Rev.*, **145**, 1717–1738, https://doi.org/10.1175/MWR-D-16-0350.1.

Rozoff, C. M., W. H. Schubert, and J. P. Kossin, 2008: Some dynamical aspects of tropical cyclone concentric eyewalls. *Quart. J. Roy. Meteor. Soc.*, **134**, 583–593, https://doi.org/10.1002/qj.237.

Schubert, W. H., M. T. Montgomery, R. K. Taft, T. A. Guinn, S. R. Fulton, J. P. Kossin, and J. P. Edwards, 1999: Polygonal eyewalls, asymmetric eye contraction, and potential vorticity mixing in hurricanes. *J. Atmos. Sci.*, **56**, 1197–1223, https://doi.org/10.1175/1520-0469(1999)056<1197:PEAECA>2.0.CO;2.

Shapiro, L. J., and H. E. Willoughby, 1982: The response of balanced hurricanes to local sources of heat and momentum. *J. Atmos. Sci.*, **39**, 378–394, https://doi.org/10.1175/1520-0469(1982)039<0378:TROBHT>2.0.CO;2.

Sitkowski, M., J. P. Kossin, and C. M. Rozoff, 2011: Intensity and structure changes during hurricane eyewall replacement cycles. *Mon. Wea. Rev.*, **139**, 3829–3847, https://doi.org/10.1175/MWR-D-11-00034.1.

——, ——, ——, and J. A. Knaff, 2012: Hurricane eyewall replacement cycle thermodynamics and the relict inner eyewall circulation. *Mon. Wea. Rev.*, **140**, 4035–4045, https://doi.org/10.1175/MWR-D-11-00349.1.

Smith, R. K., M. T. Montgomery, and V. S. Nguyen, 2009: Tropical cyclone spin-up revisited. *Quart. J. Roy. Meteor. Soc.*, **135**, 1321–1335, https://doi.org/10.1002/qj.428.

Stewart, S. R., 2017: Hurricane Matthew (28 September–9 October 2016). National Hurricane Center Tropical Cyclone Rep. AL142016, 96 pp., https://www.nhc.noaa.gov/data/tcr/AL142016_Matthew.pdf.

Tang, B., and K. Emanuel, 2012: A ventilation index for tropical cyclones. *Bull. Amer. Meteor. Soc.*, **93**, 1901–1912, https://doi.org/10.1175/BAMS-D-11-00165.1.

Uhlhorn, E. W., P. G. Black, J. L. Franklin, M. Goodberlet, J. Carswell, and A. S. Goldstein, 2007: Hurricane surface wind measurements from an operational stepped frequency microwave radiometer. *Mon. Wea. Rev.*, **135**, 3070–3085, https://doi.org/10.1175/MWR3454.1.

Wang, Y., 2002: Vortex Rossby waves in a numerically simulated tropical cyclone. Part II: The role in tropical cyclone structure and intensity changes. *J. Atmos. Sci.*, **59**, 1239–1262, https://doi.org/10.1175/1520-0469(2002)059<1239:VRWIAN>2.0.CO;2.

——, and G. J. Holland, 1996: Tropical cyclone motion and evolution in vertical shear. *J. Atmos. Sci.*, **53**, 3313–3332, https://doi.org/10.1175/1520-0469(1996)053<3313:TCMAEI>2.0.CO;2.

Willoughby, H. E., 1982: Concentric eye walls, secondary wind maxima, and the evolution of the hurricane vortex. *J. Atmos. Sci.*, **39**, 395–411, https://doi.org/10.1175/1520-0469(1982)039<0395:CEWSWM>2.0.CO;2.

——, and M. B. Chelmow, 1982: Objective determination of hurricane tracks from aircraft observations. *Mon. Wea. Rev.*, **110**, 1298–1305, https://doi.org/10.1175/1520-0493(1982)110<1298:ODOHTF>2.0.CO;2.